

Parametrically Excited Electrostatic MEMS Cantilever Beam With Flexible Support

Mark Pallay

Department of Mechanical Engineering,
Binghamton University,
4400 Vestal Parkway East,
Binghamton, NY 13902

Shahrazad Towfighian¹

Department of Mechanical Engineering,
Binghamton University,
4400 Vestal Parkway East,
Binghamton, NY 13902
e-mail: stowfigh@binghamton.edu

Parametric resonators that show large amplitude of vibration are highly desired for sensing applications. In this paper, a microelectromechanical system (MEMS) parametric resonator with a flexible support that uses electrostatic fringe fields to achieve resonance is introduced. The resonator shows a 50% increase in amplitude and a 50% decrease in threshold voltage compared with a fixed support cantilever model. The use of electrostatic fringe fields eliminates the risk of pull-in and allows for high amplitudes of vibration. We studied the effect of decreasing boundary stiffness on steady-state amplitude and found that below a threshold chaotic behavior can occur, which was verified by the information dimension of 0.59 and Poincaré maps. Hence, to achieve a large amplitude parametric resonator, the boundary stiffness should be decreased but should not go below a threshold when the chaotic response will appear. The resonator described in this paper uses a crab-leg spring attached to a cantilever beam to allow for both translation and rotation at the support. The presented study is useful in the design of mass sensors using parametric resonance (PR) to achieve large amplitude and signal-to-noise ratio.

[DOI: 10.1115/1.4034954]

1 Introduction

Microelectromechanical systems (MEMS) are used extensively in modern electrical, mechanical, and biological devices. With new technology becoming both more complex and space efficient, MEMS are a necessity to develop high-performance electronics. MEMS resonators are a class of dynamic MEMS devices that utilize a vibrating beam or plate for mass and pressure sensing [1], gyroscopes/motion detection [2], energy harvesting [3], and many other applications [4,5]. Their small size allows for extremely sensitive systems that consume minimal energy and have low fabrication costs. With the desire for self-powered resonators, significant effort has been made to further reduce energy consumption without sacrificing performance [3,5–7]. For many electrostatic MEMS resonators, optimization is aimed at increasing the amplitude of vibration while minimizing the excitation voltage. Large vibration amplitudes are desirable because they result in a high signal-to-noise ratio for sensors, which increases sensitivity. A low excitation voltage reduces the overall power consumption of the resonator, creating a more energy efficient sensor.

Parametric excitation (PE) has been used in MEMS resonators [3,6,8–11] due to its low threshold voltage and high amplitude of vibration at frequencies far from the natural frequency of the system [12,13]. PE refers to excitation through time-varying parameters of the system rather than through direct forcing in the direction of the desired motion [6]. This phenomenon was first noted by Faraday in the 1800s while studying the motion of fluid waves in closed cylinders [12]. In the early 1990s, Rugar and Grutter applied this principle to a MEMS cantilever resonator through a parametric amplifier and harmonic forcing [14]. Turner et al. expanded this work by classifying the parametric instability regions/tongues in 1998 [15], which has laid the groundwork for parametrically excited MEMS resonator designs.

The most common method of PE involves imposing a time-varying force in one direction to amplify a vibration in a perpendicular direction. In MEMS sensors, this is achieved in a two degrees-of-freedom (DOF) system where one direction of

vibration is dedicated to sensing, and a perpendicular direction is used for actuation [2]. If the actuator is driven at a frequency within an instability tongue of the system, it can drive the sensing direction into resonance. Another way of achieving PR in MEMS is to modulate the effective stiffness of the resonator with time, using piezoelectrics, magnetism, or electrostatics [6]. In electrostatic MEMS, the effective stiffness is dependent on both the mechanical stiffness of the beam and the electrostatic forces between the beam and electrode. If the stiffness is modulated in a way such that the restoring force of the beam is smaller when it deflects away from the equilibrium point compared to when it returns, the beam can show large oscillations (PR). The oscillations reach steady-state when the beam has deflected far enough that the mechanical restoring force of the beam dominates and prevents the beam from deflecting further at the applied voltage.

The effect of flexible supports, on the other hand, has been extensively studied for MEMS beams. In 2000, Kobrinsky et al. [16] developed an analytical model for a clamped-clamped electrostatic microbeam that takes into account support compliance. This was used to help explain initial beam deflections that had a significant effect on the dynamic response of the beam. Pakdemirli and Boyaci [17] studied the effect of a flexible boundary on the natural frequency and steady-state amplitude of several beam types. It was shown that flexible supports may either increase or decrease both the natural frequency and steady-state amplitude, depending on the nature of the boundary conditions. Rinaldi et al. [18] created a model for a cantilever microbeam with nonideal supports. Comparisons between the ideal and nonideal boundary for the cantilever, regarding static tip deflection and natural frequency, were conducted. Clamped-Clamped arches with nonideal supports were investigated by Alkharabsheh and Younis [19,20]. Further research of the dynamic effect of nonideal boundary conditions for various types of beams has been reported in Refs. [21–23].

A major obstacle for MEMS electrostatic resonators is the pull-in instability that severely limits their range of motion. This occurs when the electrostatic forces pulling electrodes together overcome the mechanical forces separating them and the beam collapses to the electrode. For dynamic MEMS, such as resonators, this phenomenon occurs at even lower voltages (dynamic pull-in) than if the devices were operated statically. The pull-in voltage ultimately depends on the geometry of the resonator;

¹Corresponding author.

Contributed by the Technical Committee on Vibration and Sound of ASME for publication in the JOURNAL OF VIBRATION AND ACOUSTICS. Manuscript received April 21, 2016; final manuscript received September 19, 2016; published online December 7, 2016. Assoc. Editor: Izhak Bucher.

however, in most cases, the beam can only reach from 33% to 50% of the gap distance before pull-in occurs. Since electrostatic forcing is inherently nonlinear, the beam must be close to the electrode to increase the magnitude of the force. This can yield pull-in voltages under 2 V for cantilever beams that are in close proximity to the electrode [12].

Utilizing electrostatic fringe fields, Linzon et al. [6] investigated a MEMS parametric resonator that does not suffer from pull-in instability. The system contained a long, thin cantilever beam surrounded by an electrode at its free end. In their study, the electrostatic force acts as a restoring force, whose stiffness is a function of alternating current (AC) voltage and varies with time. Varying the stiffness with time drives the beam into parametric resonance. Large vibration amplitudes have been achieved; however, because the fringe field generates a weak electrostatic field, the threshold voltage necessary to induce parametric resonance is high.

The contribution of this paper is to reduce the threshold voltage of a fringe field MEMS parametric resonator while maintaining a high vibration amplitude to increase the signal-to-noise ratio. This is achieved by adding a flexible support to the resonator as shown in Fig. 1. Many resonators, including the one in Ref. [6], use fixed supports. Fixed supports require the beam to bend to deflect from the equilibrium point, which is a severe limitation on the vibration amplitude of the beam because of the nonlinear stiffness at large deformations. The flexible support allows for rotation and translation at the fixed boundary, yielding less overall resistance to the deflection of the beam. This design can theoretically achieve higher amplitudes at lower voltages because it allows for a deflection without bending the beam. As bending of the beam is what dominates the restoring force at high amplitudes, the less the beam bends, the smaller the restoring force. With a lower restoring force at any given deflection, the beam can deflect to a larger amplitude under the same magnitude of electrostatic force. Unlike previous studies on nonideal supports [19–23], which justified dynamic behaviors by modeling the base with springs attached, we purposely added a flexible support to increase vibration amplitudes.

The flexible support is achieved by adding a crab-leg spring at the fixed end of the cantilever. This configuration is chosen because it allows for easy control of both the translational and rotational stiffness. This is used over a serpentine configuration (the typical MEMS torsional spring) because the torsional stiffness of the serpentine spring is much lower than translational stiffness, while a balance between the two is needed to create large amplitudes (refer to Sec. 2.3). We demonstrate that decreasing the boundary stiffness below a threshold results in a chaotic response, which should be avoided if the resonator is used as a sensor.

The organization of this paper is as follows: Section 2 outlines the derivation of the theoretical model with the added flexible

support, as well as the simulation results. In Sec. 3, a physical model and results are discussed. The final conclusions based on the physical model's results are given in Sec. 4.

2 Theoretical Model

2.1 Equation of Motion. The governing equation of motion for the beam is obtained using Euler–Bernoulli beam theory. The dimensions of the beam are given in Table 1. The beam material is a single crystal silicon and assumed to be linearly elastic. This model assumes only deflection in the z -direction, with no axial/lateral displacement and no twisting of the beam. Therefore, the z -displacement of the beam is only dependent on the position along the beam (\hat{x}) and time (\hat{t}). The dimensionalized equation of motion (denoted by \hat{w}) is shown in the below equation

$$\rho A \frac{\partial^2 \hat{w}}{\partial \hat{t}^2} + \hat{c} \frac{\partial \hat{w}}{\partial \hat{t}} + EI \frac{\partial^4 \hat{w}}{\partial \hat{x}^4} + \hat{f}_e V^2 = 0 \quad (1)$$

In Eq. (1), \hat{f}_e denotes the electrostatic force on the beam from the electrode. The analytical expression of this force was determined in Ref. [6] by using a fitting expression from a finite-element simulation. We verified the fitting expression by making a COMSOL simulation of the two-dimensional section of the electrode

$$\hat{f}_e(\hat{w}) = \frac{a \sinh\left(\sigma \frac{\hat{w}}{h}\right)}{\cosh^p\left(\sigma \frac{\hat{w}}{h}\right)} H(\hat{x} - \hat{x}_e) \quad (2)$$

In Eq. (2), a , σ , and p are the fitting parameters that depend on the geometry of the beam, and H is the Heaviside step function, with the values of the fitting parameters given in Table 1.

Equation (1) is first nondimensionalized. These substitutions are as follows:

$$\begin{aligned} x &= \hat{x}/L \\ g &= \hat{g}/h \\ w &= \hat{w}/h \\ t &= \hat{t} \sqrt{EI/\rho AL^4} \\ c^* &= \hat{c} \sqrt{L^4/EI\rho A} \\ f_e &= \hat{f}_e/a \\ \beta &= aL^4 V_0^2 / EIh \end{aligned}$$

β is a new nondimensional parameter that represents the constant coefficients of the electrostatic forcing function. The nondimensional equation of motion is shown in the below equation

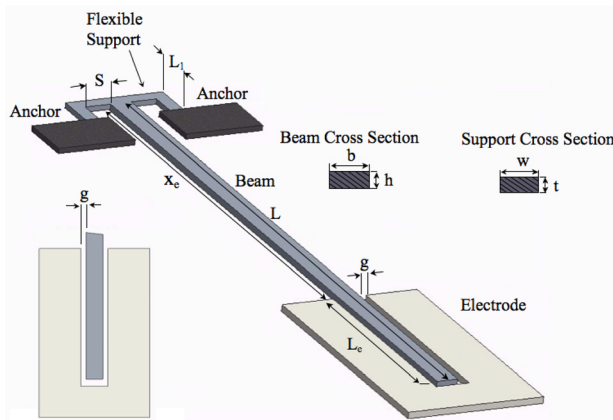


Fig. 1 Layout of the resonator with cross section of the beam and top down view of electrode and beam tip

Table 1 Beam parameters of MEMS resonator given in Ref. [6]

Parameter	Symbol	Value
Beam length (μm)	L	500
Beam width (μm)	b	16
Beam height (μm)	h	5
Electrode gap (μm)	g	5
Electrode length (μm)	L_e	150
Elastic modulus (GPa)	E	169
Density (kg/m^3)	ρ	2330
Poisson's ratio	ν	0.3
Quality factor	Q	150
Fitting parameter	a	1.3×10^{-6}
Fitting parameter	σ	1
Fitting parameter	p	1.45

$$\frac{\partial^2 w}{\partial t^2} + c^* \frac{\partial w}{\partial t} + \frac{\partial^4 w}{\partial x^4} + \beta V^2 f_e = 0 \quad (3)$$

In both the nondimensional substitutions and Eq. (3), the nonaccented variables denote the nondimensional quantities. Equation (3) is then solved using the Galerkin decomposition procedure. Using this method, the deflection of the beam is approximated as

$$w(x, t) \approx \sum_{i=1}^n q_i(t) \phi_i(x) \quad (4)$$

where $\phi_i(x)$ are the mode shapes of the beam, and $q_i(t)$ are the time-dependent generalized coordinates, which must be solved numerically. The mode shapes can be obtained by solving the eigenvalue problem associated with Eq. (3) as will be described in Sec. 2.2. Once the mode shapes are obtained, one can substitute Eq. (4) into the nondimensionalized equation of motion (Eq. (3)), multiply by ϕ_i , and integrate over x between 0 and 1 to get

$$m_i \ddot{q}_i + c^* m_i \dot{q}_i + k_i q_i + \beta V^2 f_i = 0 \quad (5)$$

This is done to reduce the partial differential equation (PDE) into a set of decoupled ordinary differential equations (ODE) using the orthogonality of the mode shapes. In Eq. (5), m_i , k_i , and f_i are defined in Eq. (10).

2.2 Flexible Support. The addition of a flexible support is taken into account by the mode shapes of the beam ($\phi(x)$). Specifically, this introduces a new set of boundary conditions for $\phi(x)$ given below [12]. Figure 2 shows the comparison between the flexible and fixed support

$$\begin{aligned} \phi''(0) - \frac{Lk_r}{EI} \phi'(0) &= 0 \\ \phi'''(0) - \frac{L^3 k_t}{EI} \phi'(0) &= 0 \\ \phi''(L) &= 0 \\ \phi'''(L) &= 0 \end{aligned} \quad (6)$$

In Eq. (6), k_r and k_t are the rotational and translational stiffness of the flexible boundary, respectively. Two nondimensional variables, R_r and R_t , are defined for simplicity and are shown in the below equation

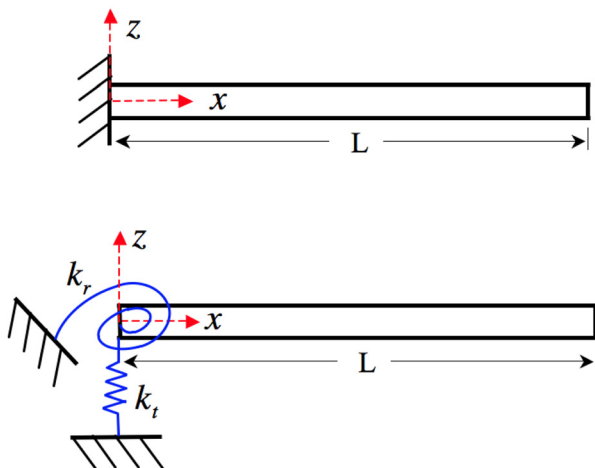


Fig. 2 Fixed versus flexible support

$$R_r = \frac{Lk_r}{EI} \quad R_t = \frac{L^3 k_t}{EI} \quad (7)$$

Once the boundary conditions have been defined, the mode shapes can be computed. This is done by setting both the voltage and damping of Eq. (3) equal to zero, and using the Galerkin procedure (separation of variables) to reduce the PDE into two ODEs. A generalized mode shape

$$\begin{aligned} \phi &= A \cos(\alpha x) + B \sin(\alpha x) \\ &+ C \cosh(\alpha x) + D \sinh(\alpha x) \end{aligned} \quad (8)$$

is used, where A , B , C , and D are the constants, and α is the square root of the nondimensional natural frequency. Substituting this back into the boundary conditions of Eq. (6) yields the system of equations shown in the below equation

$$\begin{bmatrix} -\alpha & -R_r & \alpha & -R_r \\ R_t & -\alpha^3 & R_t & \alpha^3 \\ -\cos(\alpha L) & -\sin(\alpha L) & \cosh(\alpha L) & \sinh(\alpha L) \\ \sin(\alpha L) & -\cos(\alpha L) & \sinh(\alpha L) & \cosh(\alpha L) \end{bmatrix} \begin{bmatrix} A \\ B \\ C \\ D \end{bmatrix} = 0 \quad (9)$$

For a nontrivial solution, the determinant of the matrix on the left side must be zero, which yields a characteristic equation for α , the eigenvalue. Solving numerically, the eigenvalues are obtained and used in Eq. (9) to find A , B , C , and D . Mode shape, ϕ , is then normalized to have a maximum of one. Using these mode shapes and the orthogonality condition, one can obtain the coefficients of m_i , k_i , and f_i in the decoupled equation of motion (Eq. (5))

$$\begin{aligned} m_i &= \delta_{ij} \int_0^1 \phi_j \phi_i dx \\ k_i &= \delta_{ij} \int_0^1 \phi_j \phi_i^{IV} dx \\ f_i &= \int_{x_e}^1 f_e \phi_j dx \end{aligned} \quad (10)$$

where δ_{ij} is the Kronecker delta, which is zero when $i \neq j$, and one when $i = j$. Equation (5) is then solved numerically in MATLAB using the fourth-order Runge–Kutta method with the ODE45 solver [24].

2.3 Numerical Results. The effect of the flexible support on the parametric resonance of the beam was studied for a one-mode model. The damping was estimated as

$$c = \frac{\lambda_1^2}{Q} \quad (11)$$

where $c = c^* m_1$ in Eq. (5) for a one-mode model. In Eq. (11), λ_1^2 is the first natural frequency of the cantilever and the flexible support, and Q is the quality factor. The quality factor experimentally determined in Ref. [6] for the fixed support was used in Eq. (11) as an estimate. This value was chosen due to the similarity between the two resonators when the boundary stiffness is sufficiently large. It should also be noted that due to the single layer design of the beam and electrode, squeeze film damping is almost eliminated, and a major part of the total damping is due to viscous and support damping. It is assumed that the change in support damping as boundary stiffness decreases can be roughly accounted for by Eq. (11). This can be visualized in the damping profile of Fig. 3.

The beam was also given a very small initial offset to initiate parametric resonance. This is necessary because when the beam is not deflected, the net electrostatic force is zero.

To verify the accuracy of the presented model, first R_r and R_t were set to 10,000. At $R_r = R_t = 10,000$ and above, the rotation

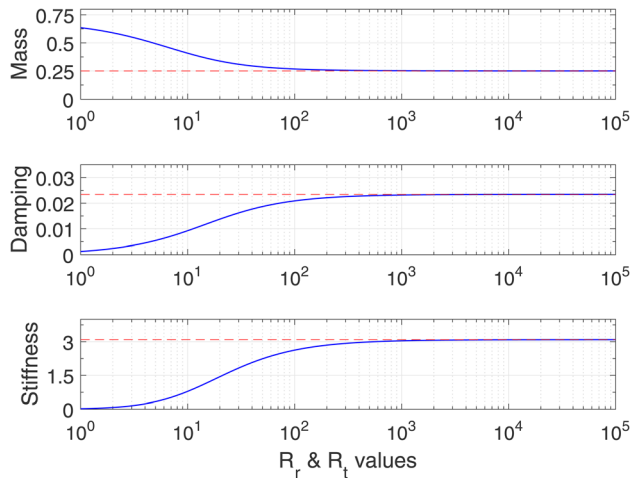


Fig. 3 The convergence of nondimensional mass (m), damping (c), and stiffness (k) values to the fixed boundary case (dashed lines) as R_r and R_t increase. Good convergence occurs at approximately 10^4 and above.

and translation of the flexible boundary are negligible and the beam behaves like a simple cantilever. This was determined by plotting m , c , and k values for increasing boundary stiffness and looking for convergence to the m , c , and k values for the fixed boundary. Figure 3 shows this convergence to those of the fixed support reported in Ref. [6].

To study the effect of a rotational and translational spring at the support, three cases are investigated. First, R_r is decreased while R_t is held fixed (case I). This is the equivalent of a pure rotational spring with no translational movement of the supported end. Next, R_t is varied and R_r is held fixed (case II), which is similar to an ideal translational spring. Finally, R_r and R_t are equated and analyzed at different values to simulate the complete flexible support (case III). The frequency response for cases I, II, and III, at 100 V AC can be seen in Figs. 4–6, respectively.

All the three cases have similar effects on the frequency response domain with case III being the most pronounced. First, there is a significant downward shift in the frequency response due to the reduction of the overall stiffness of the system. Second, the maximum amplitude increases when the boundary stiffness decreases up until R_r and/or R_t reach a threshold. An increase of

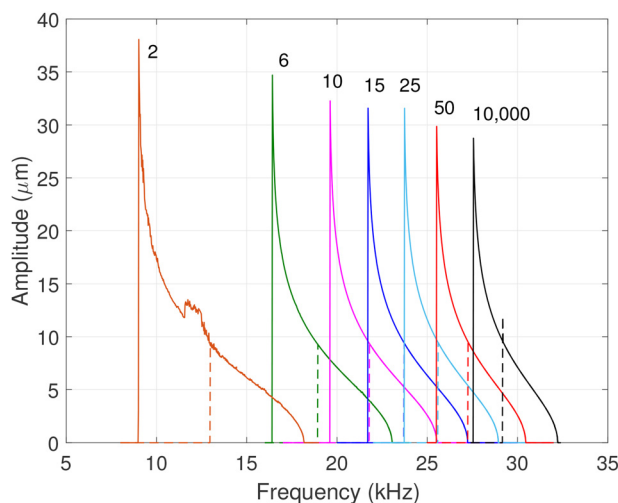


Fig. 4 Case I: R_r frequency response ($R_t = 10,000$) at 100 V AC. Numbers next to lines indicate the value of R_r . Solid lines indicate downsweep and dashed lines indicate upsweep. Frequency step of 20 Hz.

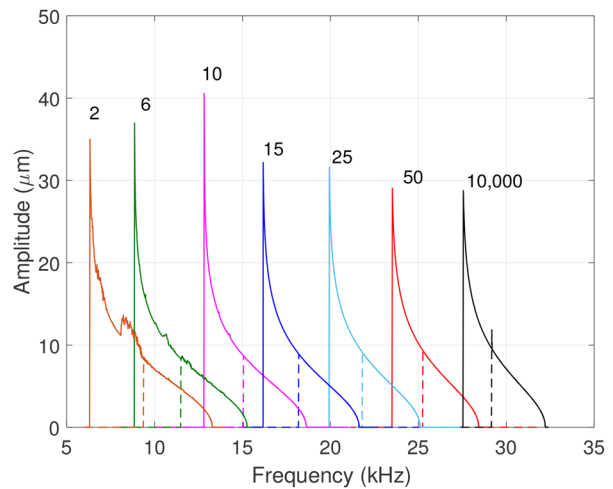


Fig. 5 Case II: R_t frequency response ($R_r = 10,000$) at 100 V AC. Numbers next to lines indicate the value of R_t . Solid lines indicate downsweep and dashed lines indicate upsweep. Frequency step of 20 Hz.

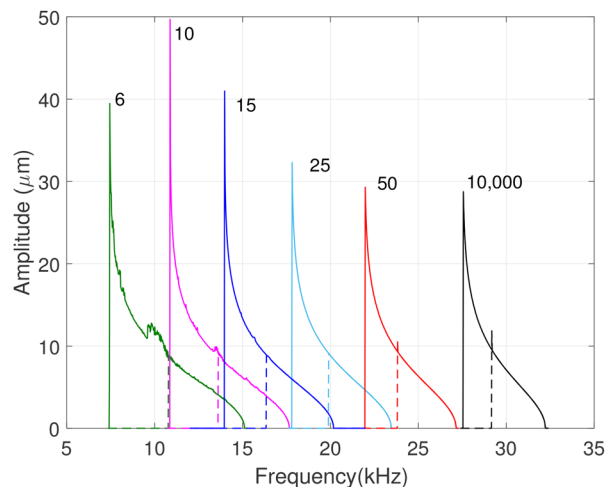


Fig. 6 Case III: $R_r = R_t$ frequency response at 100 V AC. Numbers next to lines indicate the value of R_r and R_t . Solid lines indicate downsweep and dashed lines indicate upsweep. Frequency step of 20 Hz.

66% in the maximum amplitude is observed when the stiffness reaches the threshold value ($50 \mu\text{m}$ at $R_r = R_t = 10$ compared to $30 \mu\text{m}$ at $R_r = R_t = 10,000$ for the fixed support). A time response at its maximum amplitude in Fig. 6 is shown in Fig. 7. Below the threshold value, the response becomes either odd period or chaotic (depending on the frequency) as will be discussed shortly. This can be seen in Figs. 4–6 when the frequency response curve, obtained from the maximum amplitude, is no longer smooth and appears jagged. If R_r and R_t are decreased further, the response becomes completely chaotic and does not reach steady-state.

The frequency range where parametric resonance is spread is also increased as R_r and/or R_t is decreased. At $R_r = R_t = 10$, the range is about 7000 Hz compared to about 5000 Hz for the fixed boundary. Higher-order parametric resonances were also observed as the stiffness varies (not shown in Figs. 4–6). Figure 8 shows the higher-order parametric resonances for the case of $R_r = R_t = 10$. As shown in Fig. 8, higher-order parametric resonances occur at 6.75 kHz, 4.5 kHz, and 3.375 Hz, respectively. We observed that higher-order parametric resonances move closer to the primary resonance as the boundary stiffness is decreased.

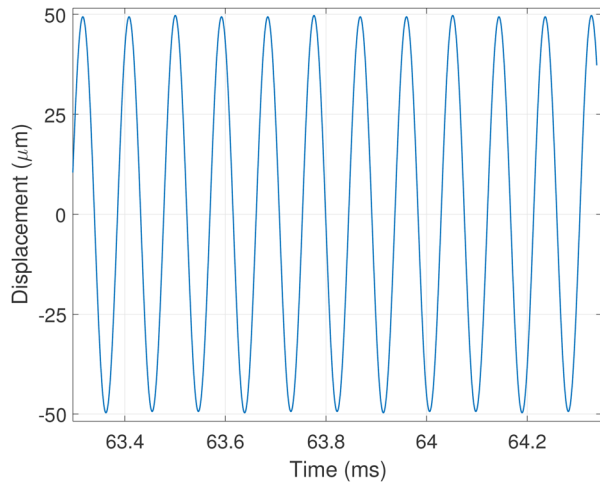


Fig. 7 $R_r = R_t = 10$ time response in steady-state regime with an approximately $50 \mu\text{m}$ amplitude. Driven at $10,880 \text{ Hz}$ at a voltage of 100 V . An initial displacement of $40 \mu\text{m}$ was used to reach the higher energy state in the backsweep region.

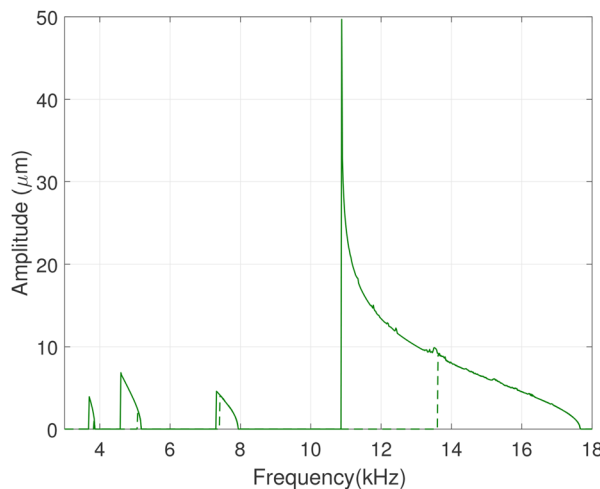


Fig. 8 Frequency response of $R_r = R_t = 10$ showing higher-order parametric resonances. Frequency step of 20 Hz .

There are slight differences between the three cases. Case I does not increase the amplitude as much as case II or III. Case II has some increase in maximum amplitude but not as large as case III. Even though all the three cases experience a chaotic response when the boundary stiffness goes below a threshold, the chaotic attractor is the largest in case II, meaning the translational stiffness has a larger effect on the size of the chaotic attractor compared to the rotational stiffness.

As mentioned above, in all the three cases, the response of the resonator becomes chaotic when the boundary stiffness goes below a threshold. Around the threshold stiffness, a small variation in peak amplitude of the steady-state response appears. Decreasing the boundary stiffness below the threshold causes the variation to become more apparent and chaotic response occurs.

To verify that the response has a chaotic nature, we plotted the bifurcation diagram for the last 50 cycles. The bifurcation diagrams shown in Figs. 9 and 10 are plotted for $R_t = 10,000$, $R_r = 2$, and $R_r = 25$, respectively. The diagram is obtained from recording the positive displacement as the phase portraits cross the zero velocity axis. As shown in Fig. 9, in certain regions of the bifurcation diagram, the chaotic attractor size is large. While other areas of the curve seem periodic, the chaotic attractor is just

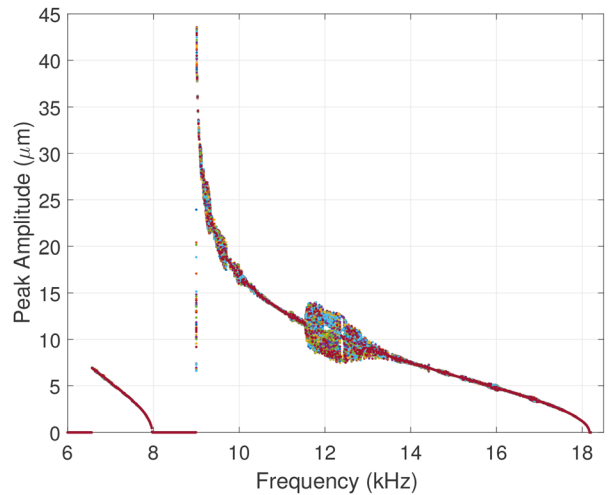


Fig. 9 Bifurcation diagram for $R_t = 10,000$ and $R_r = 2$ showing peak amplitude against frequency for the last 50 cycles in the steady-state regime. Backsweep only. Includes both primary and fundamental parametric resonances. Frequency step of 10 Hz .

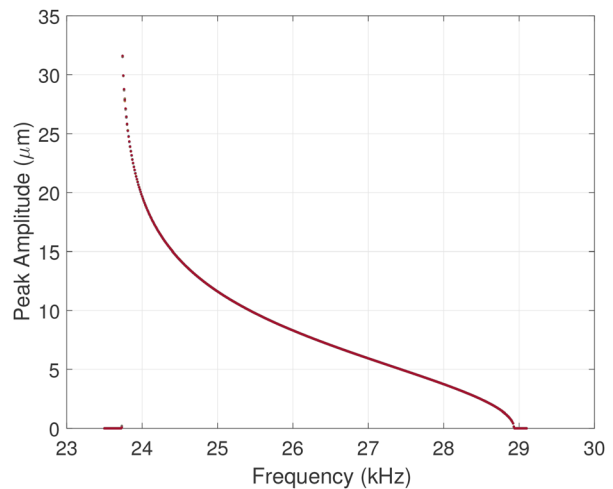


Fig. 10 Bifurcation diagram for $R_t = 10,000$ and $R_r = 25$ showing peak amplitude against frequency for the last 50 cycles in the steady-state regime. Backsweep only. Frequency step of 10 Hz .

smaller in size. In fact, for most of the resonant frequency curve, in the case of $R_r = 2$ (Fig. 9), the motion is chaotic. As the boundary stiffness is increased, the chaotic behavior disappears as can be seen in Fig. 10.

To prove that the motion is indeed chaotic, the information entropy and dimension were calculated. Information entropy calculates the unpredictability of a system. For a nonchaotic, deterministic system, the information entropy is zero because the system is fully predictable. The information dimension, calculated from the information entropy, is a quantitative measure of the fractal behavior of the attractor. Noninteger values of the information dimension show that the attractor is strange, while a nonzero information entropy shows a loss of predictability of the system, indicating chaos [25].

To calculate the information entropy and dimension, a Poincaré section was taken by sampling points at the excitation frequency starting at the maximum displacement of the last cycle (Fig. 11). The Poincaré section of the attractor was then divided into small squares of nondimensional size 0.002×0.002 . The number of

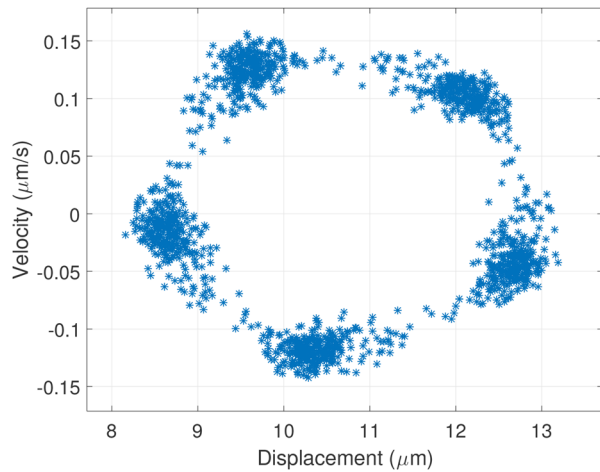


Fig. 11 Poincaré section of the chaotic attractor for $R_t = 10,000$, $R_r = 2$, and $f = 12$ kHz. A total of 1500 points were sampled. The simulation was run for 2000 cycles, with sample points starting after cycle 500 to ensure the system was on the chaotic attractor and had negligible transient effects.

points that fall in each square was counted and divided by the total number of sample points to calculate the probability of a point landing in that square for the set of data. This probability distribution was used with Eq. (12) to calculate the information entropy [25]

$$I(\varepsilon) = - \sum_{i=1}^N P_i \log P_i \quad (12)$$

In Eq. (12), N is the total number of squares in the phase plane, ε is the area of one square, and P_i is the probability for the i th square. The information entropy was then used in Eq. (13) to find the information dimension

$$d_i = - \frac{I(\varepsilon)}{\log \varepsilon} \quad (13)$$

Figure 12 shows the information dimension for various initial conditions for the case of $R_t = 10,000$ and $R_r = 2$. The information dimension is approximately 0.586. As this is a noninteger value, the attractor is shown to exhibit fractal behavior. An information dimension of 0.586 also corresponds to an information entropy of approximately 10.5 bits. This proves the system is chaotic. The information dimension should be consistent for a chaotic attractor for any initial condition. Figure 12 shows that the information dimension is consistent for various initial conditions that result in motion on the chaotic attractor.

The chaotic behavior arises from the nonlinear modulation of the effective stiffness. The high compliance of the beam due to the decreasing boundary stiffness increases the influence of this nonlinearity, which ultimately results in chaos. This can be verified through experiments by measuring the information entropy of the tip deflection.

As mentioned above, the vast majority of the resonant frequency curve is chaotic. However, at certain frequencies, the motion is periodic. This shows that the system is experiencing intermittent chaos, snapping between period 1–7 motion and chaos. These n -period regions can be seen in the bifurcation diagrams and Poincaré maps. Figure 13 shows a zoomed in portion of Fig. 9, showing period 3 and 5 behaviors. Despite intermittent chaos, no period doubling was observed at the onset of chaotic motion. A time response in the period 5 region, shown in Fig. 14, illustrates the expected five distinct peaks.

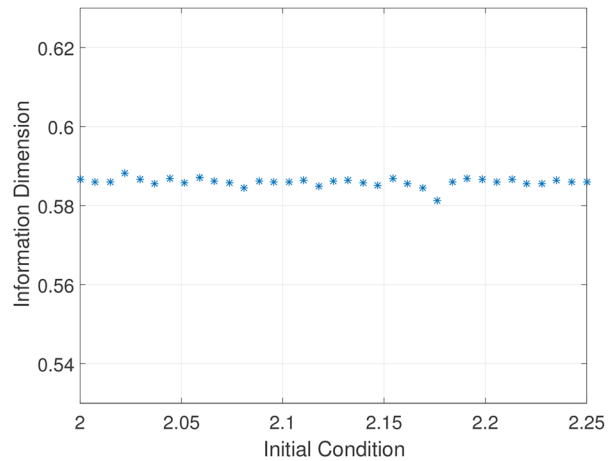


Fig. 12 Information dimension for $R_r = 2$ and $R_t = 10,000$ at $f = 12$ kHz. Initial conditions are nondimensional.

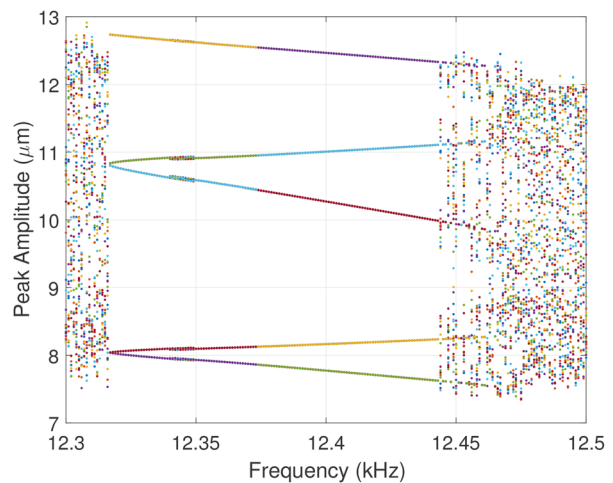


Fig. 13 Zoomed in portion of the $R_r = 2$ bifurcation diagram showing intermittent chaos and period 5 behavior. A 0.1 Hz frequency step.

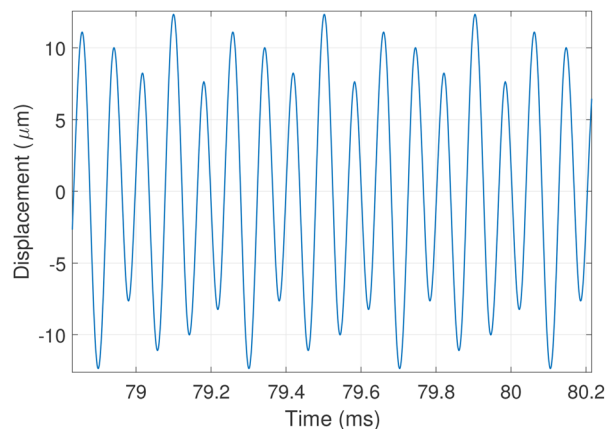


Fig. 14 Time response of $R_r = 2$ in period 5 regime at 12.44 kHz

The transition from the periodic to the chaotic region of Fig. 13 also shows other interesting behavior. The evolution of Poincaré section from period 5 to chaos is also evident in Fig. 11, which shows five prominent lumps of points that are spreading in the

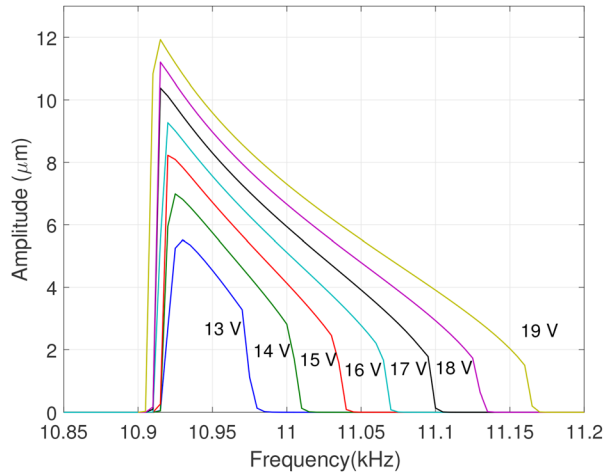


Fig. 15 Backsweep frequency response of $R_r = R_t = 10$ for low voltages. Numbers next to lines indicate voltage level. Frequency step of 5 Hz.

phase plane. As the system moves from period 5 to chaos, the variation in peak amplitude increases locally around the peak points from the period 5 regime. As the frequency is increased, these points spread out and the Poincaré section becomes more uniform and spread.

After the dynamic response was analyzed at a high voltage (100 V), it was then analyzed again at low voltages to determine its threshold for PR. Specifically, the applied voltage was incrementally increased by 1 V, starting below the threshold voltage, to see the minimum voltage required for the appearance of parametric resonance. As an example, choosing the stiffness values that resulted in the largest amplitudes in Fig. 6 ($R_r = R_t = 10$) and reducing the AC voltage yield the results shown in Fig. 15.

We recorded the lowest voltage required for parametric resonance to appear in all the three cases. Case II has the lowest threshold voltage at about 10 V. Cases I and III have a threshold voltage of 12 V and 13 V, respectively. The threshold voltage is reduced from 27 V for the fixed support case [6]. The respective threshold voltages for all the cases, including the fixed support, have the same amplitude as well (around $5 \mu\text{m}$). All the three cases significantly outperform the fixed support, even though the differences between each were slight. The flexible support also has a significant increase in amplitude at low voltages, e.g., at 16 V for case III, the flexible support has approximately the same amplitude as the fixed boundary at 40 V. However, the frequency at which parametric resonances happens for the flexible support is one-third of that of the fixed support, which decreases the rise time of the response.

Overall, case III has the most desirable effect on the frequency response achieving the highest amplitudes while still cutting the threshold voltage by over half as compared to the fixed support.

3 Flexible Support Design and Results

After the ideal model was analyzed, a physical design that could attain the results of the ideal case ($R_r = R_t = 10$) was determined. As mentioned before, a crab-leg spring was used and can be seen in Fig. 1. The rotational and translational stiffness were evaluated using Castigliano's second theorem [26] and were a function of the spring geometry

$$k_r = \left(\frac{S}{GJ} + \frac{L_1}{EI} \right)^{-1} \quad (14)$$

$$k_t = \left(\frac{L_1^3 + S^3}{3EI} + \frac{L_1 S^3}{GJ} \right)^{-1} \quad (15)$$

Table 2 Geometry and stiffness of flexible support

Parameter	Design 1	Design 2	Design 3	Design 4
S (μm)	200	100	30	30
L_1 (μm)	20	30	30	100
t (μm)	4	3	4	5
w (μm)	10	20	10	10
R_r	7.999	4.499	5.33	3.12
R_t	14.86	97.747	2203.26	206.56

In Eqs. (14) and (15), I and J are the moment of inertia and polar moment of inertia for the cross section of the spring, respectively. The stiffness values of Eqs. (14) and (15) were then substituted into Eq. (7), and nondimensional R_r was set equal to the nondimensional R_t value. This new equation was then used to find geometry that resulted in equal R_r and R_t values.

To satisfy equality of R_r and R_t , the geometry needs to be very large however. To obtain a reasonable resonator size, R_r and R_t values were unequated and given some set difference. The larger the difference between R_r and R_t , the smaller the geometry, and vice versa. Therefore, a middle ground between stiffness and geometry was found to maximize the effect of the flexible boundary, with minimal geometry.

Geometric parameters of the support, along with the resulting R_r and R_t values are shown in Table 2 for several designs, with parameters shown in Fig. 1. The material of the spring is assumed to be the same material as that of the beam.

As can be seen in Table 2, smaller length values of S result in a high translational stiffness without having much effect on the rotational stiffness, which can be confirmed from Eqs. (14) and (15). This is mainly what causes the large difference between R_r and R_t values. A small S is desirable because it determines the width and therefore the overall size of the resonator. As S is decreased, the model becomes similar to the rotational model (case I) as described above. Figure 16 shows the frequency response for design 3, and Fig. 17 shows the frequency response at low voltages, including the threshold voltage.

Compared to the fixed support, the flexible support from design 3 offers a 50% increase in the maximum amplitude ($45 \mu\text{m}$ compared to $30 \mu\text{m}$). We also observe the appearance of higher-order parametric resonances with primary resonance around 15.5 kHz. The threshold voltage was also decreased by 52% (15 V compared to 27 V).

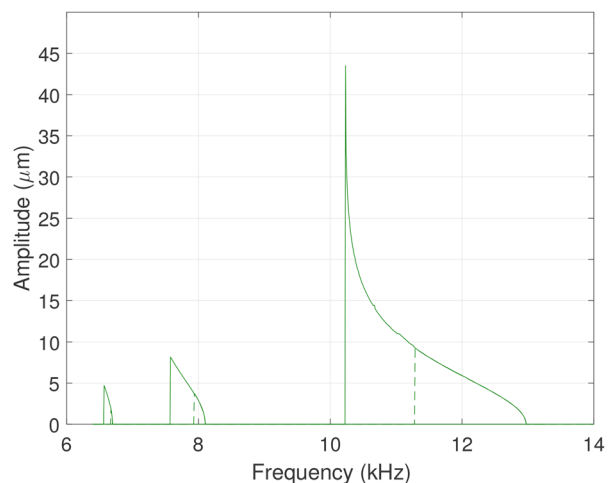


Fig. 16 Frequency response of support design 3 as listed in Table 2: $R_r = 5.33$ and $R_t = 2203.26$, at 100 V AC. Solid lines indicate downswEEP and dashed lines indicate upswEEP. Frequency step size was 20 Hz.

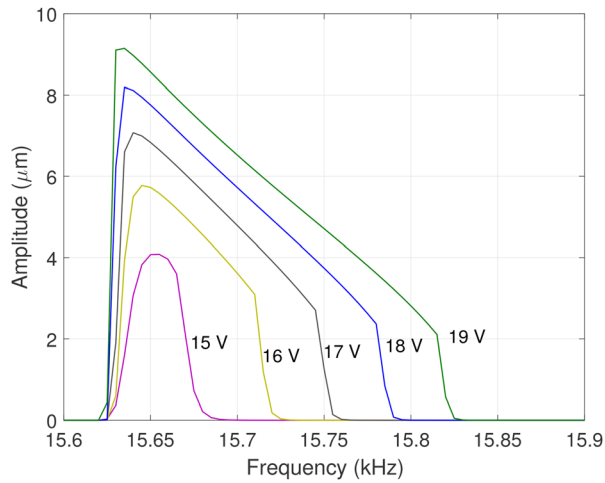


Fig. 17 Backsweep frequency response of design 3, with $R_r = 5.33$ and $R_t = 2203.26$. Numbers next to lines indicate voltage level. Frequency step of 5 Hz.

Among all the designs, design 4 that has a much smaller rotational stiffness compared to translational stiffness (similar to case I in Fig. 9) yields a chaotic response. By increasing L_1 to $100\ \mu\text{m}$, the rotational boundary stiffness drops below the threshold value, and chaos occurs. If a serpentine spring is used instead of crab-leg used here, it could result in a lower rotational stiffness and thus would be even more susceptible to a chaotic response. Although chaos could occur for case II (pure translational spring), the geometry of the resonator to create a pure translational spring at the boundary, with a stiffness below the threshold, would need to be very large and thus is unlikely to occur in a real-world MEMS device and thus not considered.

4 Conclusion

This paper demonstrates the effect of a flexible support on a parametrically excited electrostatic MEMS resonator. The resonator uses weaker electrostatic fringe fields to actuate a cantilever microbeam without the risk of pull-in, allowing for high amplitudes of vibration. The flexible support significantly decreases the threshold voltage, creating a more energy efficient resonator. The effect of boundary stiffness on the magnitude and width of the frequency response is thoroughly investigated. We observe that decreasing the boundary stiffness increases the output amplitude leading to a high signal-to-noise ratio. If the boundary stiffness is decreased below a threshold, it can yield chaotic behavior, which has been verified by the information entropy and dimension. The chaotic response may not be desired if the resonator is used as a sensor as it could complicate the sensor circuitry and hence should be avoided. A compromise needs to be made for the stiffness value to achieve the maximum amplitude and to avoid the chaotic region. An optimal design for the flexible support is described, which yields a 50% increase in the maximum amplitude and a 50% decrease in the threshold voltage for the appearance of parametric resonance.

References

- [1] Davis, Z. J., Svendsen, W., and Boisen, A., 2007, "Design, Fabrication and Testing of a Novel MEMS Resonator for Mass Sensing Applications," *Microelectron. Eng.*, **84**(5–8), pp. 1601–1605.
- [2] Sharma, M., Sarraf, E. H., and Cretu, E., 2011, "Parametric Amplification/Damping in MEMS Gyroscopes," *IEEE International Conference on Micro Electro Mechanical Systems (MEMS)*, Jan. 23–27, pp. 617–620.
- [3] Jia, Y., Yan, J., Soga, K., and Seshia, A. A., 2013, "Parametrically Excited MEMS Vibration Energy Harvesters With Design Approaches to Overcome the Initiation Threshold Amplitude," *J. Micromech. Microeng.*, **23**(11), p. 114007.
- [4] Guo, C., and Fedder, G. K., 2013, "Behavioral Modeling of a CMOS-MEMS Nonlinear Parametric Resonator," *J. Microelectromech. Syst.*, **22**(6), pp. 1447–1457.
- [5] Huang, J. M., Liu, A. Q., Deng, Z. L., and Zhang, Q. X., 2006, "A Modeling and Analysis of Spring-Shaped Torsion Micromirrors for Low-Voltage Applications," *Int. J. Mech. Sci.*, **48**(6), pp. 650–661.
- [6] Linzon, Y., Ilic, B., Lulinsky, S., and Krylov, S., 2013, "Efficient Parametric Excitation of Silicon-on-Insulator Microcantilever Beams by Fringing Electrostatic Fields," *J. Appl. Phys.*, **113**(16), p. 163508.
- [7] Frangi, A., Laghi, G., Langfelder, G., Minotti, P., and Zerbini, S., 2015, "Optimization of Sensing Stators in Capacitive MEMS Operating at Resonance," *J. Microelectromech. Syst.*, **24**(4), pp. 1077–1084.
- [8] Shmulevich, S., Grinberg, I. H., and Elata, D., 2015, "A MEMS Implementation of a Classical Parametric Resonator," *J. Microelectromech. Syst.*, **24**(5), pp. 1285–1292.
- [9] Harish, K. M., Gallacher, B. J., Burdess, J. S., and Neasham, J. A., 2008, "Experimental Investigation of Parametric and Externally Forced Motion in Resonant MEMS Sensors," *J. Micromech. Microeng.*, **19**(1), p. 015021.
- [10] Zhang, W.-M., and Meng, G., 2007, "Nonlinear Dynamic Analysis of Electrostatically Actuated Resonant MEMS Sensors Under Parametric Excitation," *IEEE Sens. J.*, **7**(3), pp. 370–380.
- [11] Welte, J., Kniffka, T. J., and Ecker, H., 2013, "Parametric Excitation in a Two Degree of Freedom MEMS System," *Shock Vib.*, **20**(6), pp. 1113–1124.
- [12] Younis, M. I., 2011, *MEMS Linear and Nonlinear Statics and Dynamics*, Springer, New York.
- [13] Krylov, S., Harari, I., and Cohen, Y., 2005, "Stabilization of Electrostatically Actuated Microstructures Using Parametric Excitation," *J. Micromech. Microeng.*, **15**(6), pp. 1188–1204.
- [14] Rugar, D., and Grütter, P., 1991, "Mechanical Parametric Amplification and Thermomechanical Noise Squeezing," *Phys. Rev. Lett.*, **67**(6), pp. 699–702.
- [15] Turner, K. L., Miller, S. A., Hartwell, P. G., MacDonald, N. C., Strogatz, S. H., and Adams, S. G., 1998, "Five Parametric Resonances in a Microelectromechanical System," *Nature*, **396**(6707), pp. 149–152.
- [16] Kobrinisky, M. J., Deutsch, E. R., and Senturia, S. D., 2000, "Effect of Support Compliance and Residual Stress on the Shape of Doubly Supported Surface-Micromachined Beams," *J. Microelectromech. Syst.*, **9**(3), pp. 361–369.
- [17] Pakdemirli, M., and Boyaci, H., 2002, "Effect of Non-Ideal Boundary Conditions on the Vibrations of Continuous Systems," *J. Sound Vib.*, **249**(4), pp. 815–823.
- [18] Rinaldi, G., Packirisamy, M., and Stiharu, I., 2008, "Boundary Characterization of MEMS Structures Through Electro-Mechanical Testing," *Sens. Actuators, A*, **143**(2), pp. 415–422.
- [19] Alkharabsheh, S. A., and Younis, M. I., 2013, "Dynamics of MEMS Arches of Flexible Supports," *J. Microelectromech. Syst.*, **22**(1), pp. 216–224.
- [20] Alkharabsheh, S. A., and Younis, M. I., 2011, "The Dynamics of MEMS Arches of Non-Ideal Boundary Conditions," *ASME Paper No. DETC2011-48501*.
- [21] Boyaci, H., 2006, "Vibrations of Stretched Damped Beams Under Non-Ideal Boundary Conditions," *Sadhana*, **31**(1), pp. 1–8.
- [22] Rinaldi, G., Packirisamy, M., and Stiharu, I., 2007, "Quantitative Boundary Support Characterization for Cantilever MEMS," *Sensors*, **7**(10), pp. 2062–2079.
- [23] Zhong, Z. Y., Zhang, W. M., and Meng, G., 2013, "Dynamic Characteristics of Micro-Beams Considering the Effect of Flexible Supports," *Sensors*, **13**(12), pp. 15880–15897.
- [24] MathWorks, 2016, "MATLAB Function Reference," MathWorks, Natick, MA, pp. 6613–6614.
- [25] Moon, F. C., 1992, *Chaotic and Fractal Dynamics*, Wiley Interscience, New York.
- [26] Budynas, R., and Nisbett, K., 2011, *Mechanical Engineering Design*, 9th ed., McGraw-Hill, New York.